Reviews of Electromagnetics, Vol. V, 2026
EuCAP 2026 Special Issue
DOI: 10.53792/RoE/2026/26007

Reviews of Electromagnetics
EuCAP 2026 Special Issue

A Low-Profile 3D-Printed Hollow-Core Fiber with Hybrid Cladding for D-Band

Shehab Khan Noor[1]*, Mengqin Gu[1], Sining An[2], Heike Ebendorff-Heidepriem[3], Deepak Mishra[1], Shaghik Atakaramians[1]*

Abstract
This paper presents the design, fabrication, and experimental validation of a compact 3D-printed hollow-core antiresonant fiber with hybrid dielectric–metal cladding for D-band (0.13–0.17 THz) applications. The metallic outer coating enhances confinement by reflecting leaking fields back into the core, thereby reducing propagation loss. The proposed fiber, fabricated using Topas and wrapped with an aluminium layer, exhibits five antiresonant transmission bands across 0.1–1 THz. With an outer diameter of 4.88 mm, the fiber achieves simulated and measured losses of 5.6 dB/m and 11.9 dB/m at 0.158 THz, respectively. Numerical analysis shows a group delay of 4.16 $\pm$ 0.81 ns and an air-core power fraction exceeding 88%. The proposed design demonstrates the smallest reported normalized core size (D_{core}/λ = 1.89 at 0.158 THz) among 3D-printed THz fibers, offering a promising solution for compact terahertz interconnects.

Key terms
Hollow-core polymer fibers; 3D printing; Antiresonant fiber; THz waveguides; Dielectric waveguides

[1] *Terahertz Innovation Group, School of Electrical Engineering and Telecommunications, UNSW Sydney, NSW 2052, Australia*
[2] *Ericsson AB, Gothenburg, Sweden*
[3] *School of Physics, Chemistry and Earth Sciences, Institute for Photonics and Advanced Sensing, Adelaide University, Adelaide, SA 5005, Australia*
*__Corresponding author__: shehab_khan.noor@unsw.edu.au, s.atakaramians@unsw.edu.au

Received: 19/06/2026, Accepted: 28/10/2026, Published: 11/11/2026

1. Introduction

The sub-terahertz (sub-THz) range, from 0.1 THz to 0.3 THz, and is considered a promising candidate for next-generation communication systems because it provides a large amount of available bandwidth for ultra-fast data transfer [1]. This region can be used for applications such as mobile base stations, data centers, and inter-connects that demand ultra-high data rates and very low latency within short- to medium-range transmission [2]. However, the use of THz waves in free-space environments remains difficult because propagation is strongly affected by atmospheric attenuation, especially absorption caused by water vapour and other molecules [3]-[4], and limits THz transmissions. One practical way to reduce these transmission limitations is to guide THz signals through low-loss fibers [5]. Yet, achieving this is not straightforward, especially near the lower part of the sub-THz range, such as 0.11 to 0.17 THz (D-band), where the comparatively long wavelength makes it challenging to efficiently confine in small diameters of fibers. This issue becomes even more important as modern systems increasingly demand compact components. Therefore, THz fiber design must address not only low transmission loss but also reduced fiber size to fit in compact systems.

Conventional signal transmission methods also face important drawbacks in the sub - THz region. Metallic conductors suffer from rapidly rising ohmic loss above 0.1 THz, while solid dielectric waveguides are constrained by material absorption, particularly in polymers [6]. Although optical fiber technology performs well in many scenarios, including high-speed transmission and broader bandwidth, it is generally not an economical solution for short- to medium-reach links (a few centimeters to 10s of meters), since the required electrical-to-optical conversion adds high cost [7]. For these reasons, hollow-core dielectric fibers present a compelling alternative, with the potential to avoid many of the limitations associated with coaxial copper cables, solid dielectric guides, and even conventional optical-fiber-based approaches in short- and medium-distance

communication systems.

In hollow-core fibers (HCF), light primarily propagates through the air core and remains largely confined within it, benefiting from a refractive index close to 1. When light travels through bulk material in a solid-core fiber, it cannot achieve the same propagation speed as in air or vacuum, which makes HCF superior to solid-core fiber [8]. Antiresonant hollow-core fibers have become increasingly popular in recent years due to their advantages, such as low loss, ease of design and fabrication, a wider bandwidth, and ease of modification compared to metallic HCF and photonic bandgap (PBG) HCF [9]. Antiresonant hollow-core fibers work on the guiding mechanism called anti-resonant reflecting optical waveguide (ARROW), where the light is confined into the air-core due to the weak coupling between the core mode and the cladding mode [10]. During resonance, light leaks from the core to the cladding, whereas during antiresonance, it is confined to the core. As a result, there are high-loss regions at certain frequencies, and between the two high-loss peaks lies a low-loss (antiresonance) region that transmits the signal.

The development of compact terahertz (THz) interconnects requires low-loss fibers that can efficiently guide THz signals for practical applications. HCFs are attractive candidates because most of the THz signal travels in the center air-core, thereby reducing material absorption loss. HCFs are relatively larger in size. In HCFs, as the core diameter decreases, optical confinement weakens and a larger fraction of the guided field leaks into the surrounding cladding, resulting in increased leakage loss. As a result, achieving both low transmission loss and compact HCFs remains a significant challenge.

Recent advances in 3D printing have enabled the fabrication of various THz HCF structures, particularly for proof-of-concept demonstrations and fundamental research, owing to the technology's rapid fabrication, low cost, and minimal space requirements. A useful parameter for understanding this trade-off is the normalized core size, D_{core}/λ, where D_{core} denotes the core diameter and λ the operating wavelength. In general, increasing D_{core}/λ enhances the fraction of power confined within the core and reduces leakage into the surrounding structure. As a result, many early designs relied on relatively large fiber dimensions to achieve acceptable performance, yet still exhibited considerable loss. For instance, Van Putten *et al.* demonstrated a polycarbonate negative curvature HCF (NC-HCF) with D_{core}/λ =12, but its measured loss at 0.3 THz remained above 100 dB/m [11]. Later studies improved the loss performance through novel geometries, including a pentagram-shaped resin-based NC-HCF with approximately 43 dB/m loss below 0.5 THz [12], a Zeonex-based AR-HCF with approximately 40 dB/m loss at 0.53 THz and reduced overall diameter [10], and a resin-based HCF with measured losses of 16 dB/m at 0.28 THz and 34 dB/m at 0.7 THz [13]. Despite these advances, most 3D-printed AR-HCFs still depend on relatively large geometries, indicating that loss reduction has largely been pursued through structural scaling rather than fundamentally new confinement strategies. In this regard, the work of Bowden *et al.* showed that a thin dielectric coating on the inner wall of a single tube HCF (ST-HCF) can significantly reduce transmission loss without complex structural modification [14]. However, fabrication methods such as extrusion and dynamic liquid-phase deposition are difficult to adapt to compact THz fiber designs. This opens the door to applying similar loss-reduction strategies in 3D-printed HCFs.

Therefore, this paper presents a 3D-printed metal-coated ST-HCF operating in the D-band (0.13–0.17 THz) using a cost-effective 3D printing approach to overcome the increased leakage associated with small-core fibers while maintaining compact diameter. Simulations and THz time domain spectroscopy (THz-TDS) system measurements confirm antiresonant low-loss guidance in the D-band, with transmission loss below 12 dB/m over a 7 GHz bandwidth (0.152–0.159 THz) for fibers with an outer diameter below 5 mm. To overcome the increased leakage associated with small-core fibers, a metallic outer coating is introduced to enhance confinement while maintaining a compact geometry. An earlier version of this paper was presented at the 20th European Conference on Antennas and Propagation (EuCAP) in 2026. This manuscript is an extended version of that work and includes several significant additions. Firstly, a detailed explanation of how the addition of a metallic layer modifies the transmission conditions in the ST-HCF, along with numerical validation, is presented in Section 2. Secondly, simulation analyses of effective refractive index of the fundamental mode, power fractions, coupling efficiencies, group delays, and dispersions. Thirdly, this expanded version provides a more comprehensive description of the 3D-printing and measurement setups, including insights into the challenges associated with the 3D-printing process and the characterization of 3D-printed Topas material. In addition, in this version, an in-depth discussion of the mismatch between simulated and measured results is included. Finally, an analysis of coupling efficiency and a detailed discussion of fiber propagation loss and coupling loss are presented.

2. Design Methodology

This section summarizes the steps of designing the proposed fiber, the numerical analysis of the metallic layer effect on fiber transmission, and the numerical results obtained for the designed fiber.

2.1. Design Principle and Metallic layer theory

The first step in designing a ST-HCF is to choose the cladding thickness (t) so that the operating frequency lies between two high-loss resonances, i.e., within the low-loss antiresonance region suitable to transmit the signal. This region is called the low-loss antiresonant region, where signals can propagate with low transmission loss. The resonance frequency (f_r) is determined by the refractive index of the dielectric material and the cladding thickness, as given by [11]:

$$f_r = \frac{m \times c}{2t\sqrt{n_{\text{t}}^2 - n_0^2}} \tag{1}$$

where c is the speed of light in a vacuumaluminium m is an integer, n_{t} is the refractive index of the cladding material, n_0 is the refractive index of fiber core (air). The addition of a metallic layer introduces a phase shift, resulting in a half-order shift in the antiresonance condition.

Topas is chosen as the host material in this work because it has the lowest absorption loss [15]. From our material characterization, the refractive index and absorption coefficient of Topas at 0.15 THz were measured to be 1.52 and 0.079 cm^{-1}, respectively [16]. Our measured material properties closely matched the results reported in [17]. Therefore, these values are used in the simulation designs as well.

The Fresnel reflection coefficient, $r = -(n_a - n_t)/(n_a + n_t)$, at an interface has the same mathematical form as the voltage reflection at a junction of two transmission lines with impedances [18, 19], while the Fresnel formulation is retained for consistency with the fiber literature in this paper. Here, n_a is the refractive index of the aluminium (metallic layer). When a metallic layer is present, since $n_a > n_t$, the Fresnel reflection coefficient becomes negative ($r < 0$), introducing a π phase shift at the polymer-metal boundary, as shown in Fig. 1 (a simplified planar-interface model rather than an exact cylindrical fiber representation). Incorporating this additional π phase shift modifies the standard thin-film interference condition [20] to:

$$\frac{4\pi t n_t}{\lambda} + \pi = 2\pi m \implies \frac{4\pi t n_t}{\lambda} = 2\pi\left(m - \frac{1}{2}\right). \quad (2)$$

Where the polymer layer thickness is denoted as t. Consequently, the resonance frequencies shift to half-integer orders ($m = 0.5, 1.5, 2.5, \ldots$), expressed as [21]:

$$f_r = \frac{(m-0.5)c}{2t\sqrt{n_t^2 - n_0^2}}. \quad (3)$$

Reflection at both the air–Topas and Topas–aluminium boundaries incurs an individual π phase shift. At a specific resonance frequency (Eq. 3), the two reflections add up to a 2π phase shift, resulting in constructive interference. This constructive superposition strongly confines the light within the core, thereby lowering overall losses through reduced leakage.

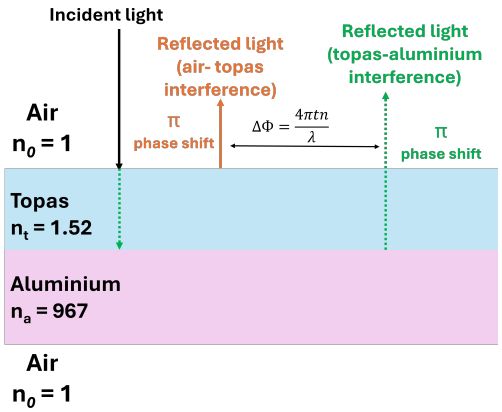
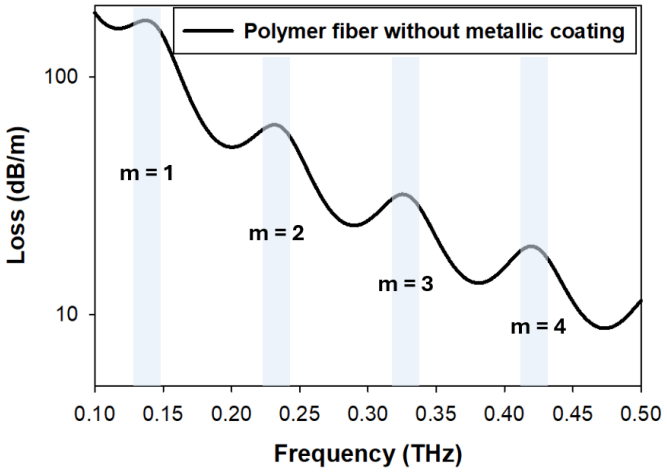
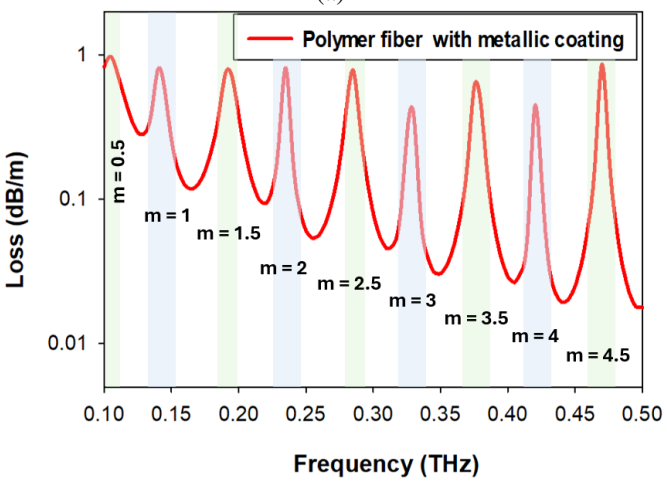


Figure 1: Phase shift of the reflected wave at the polymer–metal interface as a function of frequency.

To numerically verify the effect of metallic coating, an 8 mm outer-diameter circular HCF with 1.4 mm cladding thickness and coated with an outer aluminium layer was designed. Compared to the resonances produced by the uncoated HCF depicted in Fig. 2(a), the metallic coating introduces additional resonances between the original antiresonant bands, resulting in a narrower transmission bandwidth shown in Fig. 2(b). However, the metallic layer significantly reduces loss by nearly two orders of magnitude by reflecting leaked light back into the air core.



(a)



(b)

Figure 2: Simulated transmission loss of an 8 mm outer-diameter circular hollow-core fiber: (a) without metallic coating, showing resonance and antiresonance regions; (b) with metallic coating, showing additional resonances and reduced transmission loss.

2.2. Numerical design, geometrical optimisation and numerical results

Finite element simulations (using the commercial FEM solver COMSOL Multiphysics) are used to design the fiber. In general, copper coaxial cable diameters range from 2.54 mm to 31.75 mm [22]. Therefore, a fiber diameter of 5 mm was chosen for the proposed design to explore the feasibility of HCFs as a replacement for copper coaxial cables for short to medium-range next-generation communication systems. Based on Eq. (2), the cladding thickness was varied from 0.5 mm to 0.9 mm to

keep D-band out of resonances. Finally, a cladding thickness of 0.7 mm is chosen as it would keep the 0.11-0.17 THz within the antiresonance region.

2.2.1. Transmission loss

The structural dimensions of the proposed fiber with a metallic coating are shown in Fig. 3(a). The simulated transmission loss in the absence of a metallic coating on the outer polymer surface is illustrated in Fig. 3(b). Owing to the small D_{core}/λ ratio, the light leakage becomes significantly high, preventing the antiresonant mechanism from effectively confining light within the HCF. In contrast, when a metallic layer is introduced, as shown in Fig. 3(c), the leakage is substantially suppressed, allowing the antiresonant effect to efficiently guide and confine the light inside the core. The calculated theoretical resonances below 0.4 THz based on Topas material properties are 0.095, 0.19, 0.285, and 0.38 THz, and the resonance region is highlighted as shown in Fig. 3(c). It should be noted that the resonance formula provides only an approximation of the resonance frequency, and based on Fig. 3(c), the simulated resonances closely match the theoretical values. In the frequency range of 0.13–0.17 THz, the simulated loss was found to be between 5 and 7 dB/m. It can be further observed that as the frequency increases and the D_{core}/λ ratio increases, the loss decreases. Therefore, the loss in window 3 is lower than the loss in windows 1 and 2, as shown in Fig. 3(c). It is important to design a fiber in such a way that the frequency of interest falls under higher-order windows to have a low-loss transmission region. The effective refractive index of the fundamental mode in the first three antiresonance windows is shown in Fig. 3(d), where the resonance region is shaded with grey boxes.

2.2.2. Power fraction

The calculated air-core power fraction of the designed circular hollow-core fiber is shown in Fig. 4. The air-core power fraction increases with frequency across the antiresonance windows, indicating stronger confinement of the fundamental mode within the central air core as the normalized core size (D_{core}/λ) increases. Consequently, less power interacts with the surrounding polymer cladding, leading to reduced leakage and material absorption losses. The air-core power fraction exceeds 88% in the D-band and reaches approximately 97% in the third antiresonance window, confirming the effectiveness of the hollow-core guiding mechanism and the suitability of the proposed fiber for low-loss terahertz-wave transmission.

2.2.3. Coupling efficiency

The coupling efficiency (η) between the Gaussian beam and the fiber's fundamental mode can be determined by evaluating the overlap integral of their field distributions [23]. The coupling efficiency calculation is performed based on the equation reported in [24]. The normalized electric and magnetic field distributions3D-printed of the simulated HCF based on 3D printed dimensions are shown in Fig. 5(a) and Fig. 5(b), respectively. The Gaussian beam width was determined from measurements obtained using the TDS system with the same set of lenses used in this study. In the D-band region, specifically for 0.158 THz, η is 65 %, corresponding to a coupling loss of 1.88 dB at each fiber end. The transverse field overlap

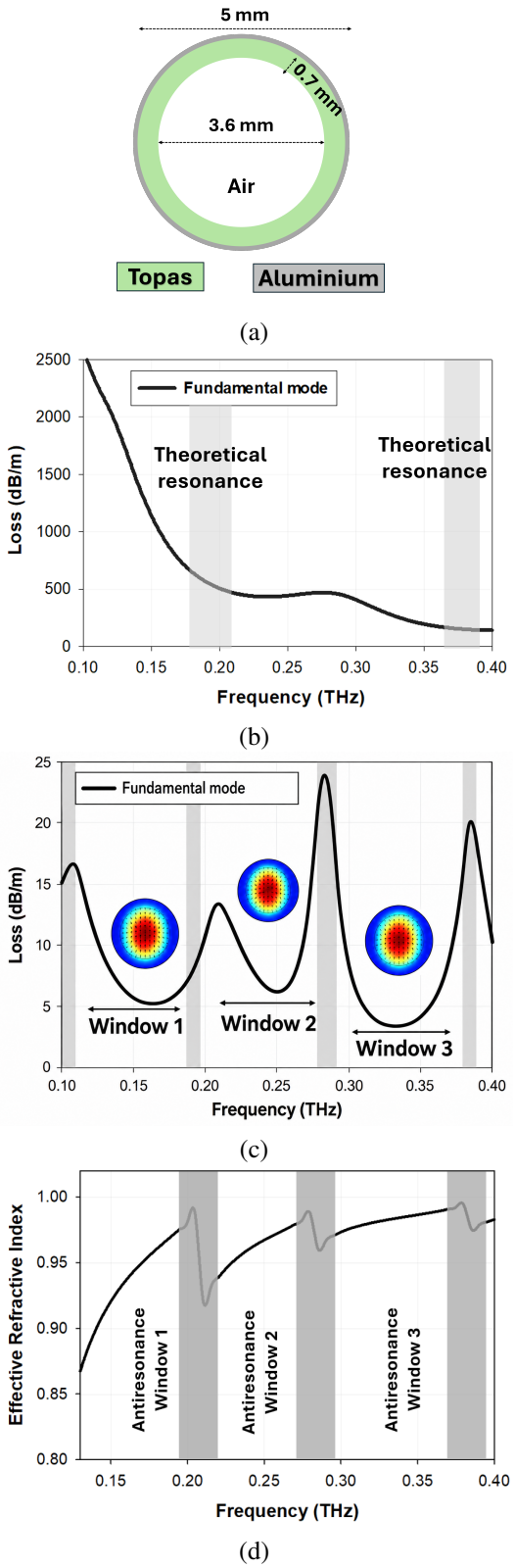


Figure 3: Proposed fiber design and simulated performance: (a) cross-sectional dimensions of the fiber; (b) transmission loss without metallic coating; (c) transmission loss with metallic coating; (d) effective refractive index of the fundamental mode.

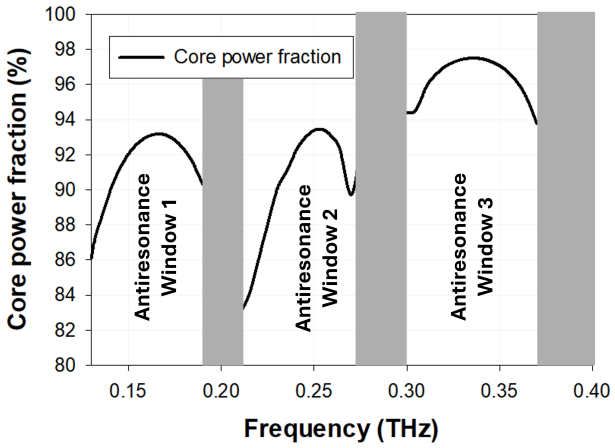


Figure 4: Simulated air-core power fraction of the designed fiber.

integral indicates a maximum coupling efficiency of 92% (η = 0.92), corresponding to a loss of 0.34 dB at each fiber end at 0.430 THz, as shown in Fig. 5(c). Note that the overall transmission loss of the fiber comprises both propagation loss and coupling loss. Therefore, reducing the coupling loss directly contributes to a decrease in the total transmission loss. A more detailed discussion is provided in Section 3 of this manuscript.

2.2.4. Group delay and Dispersion

The group delay and dispersion characteristics of the proposed fiber are presented in Fig. 6. As illustrated in Fig. 6(a), the group delay gradually decreases with increasing frequency across all three antiresonance windows. This trend arises from the increase in the normalised core diameter (D_{core}/λ), which improves the confinement of the fundamental mode within the hollow core and reduces its interaction with the cladding region. As a result, the mode propagates with a lower delay at higher frequencies. Within the frequency band of interest (antiresonance window 1), the group delay remains relatively constant, with a value of 4.16 $\pm$ 0.81 ns. The corresponding dispersion profile is shown in Fig. 6(b). As the dispersion approaches zero, the group-delay variation becomes more uniform, leading to a flatter response that is advantageous for broadband data transmission due to reduced pulse broadening and distortion. In antiresonance window 1, the dispersion is approximately -36.5 ± 20 ps/THz/cm. The relatively low variation of group delay (below 1 ns) throughout the frequency of interest indicates stable propagation characteristics with limited pulse distortion.

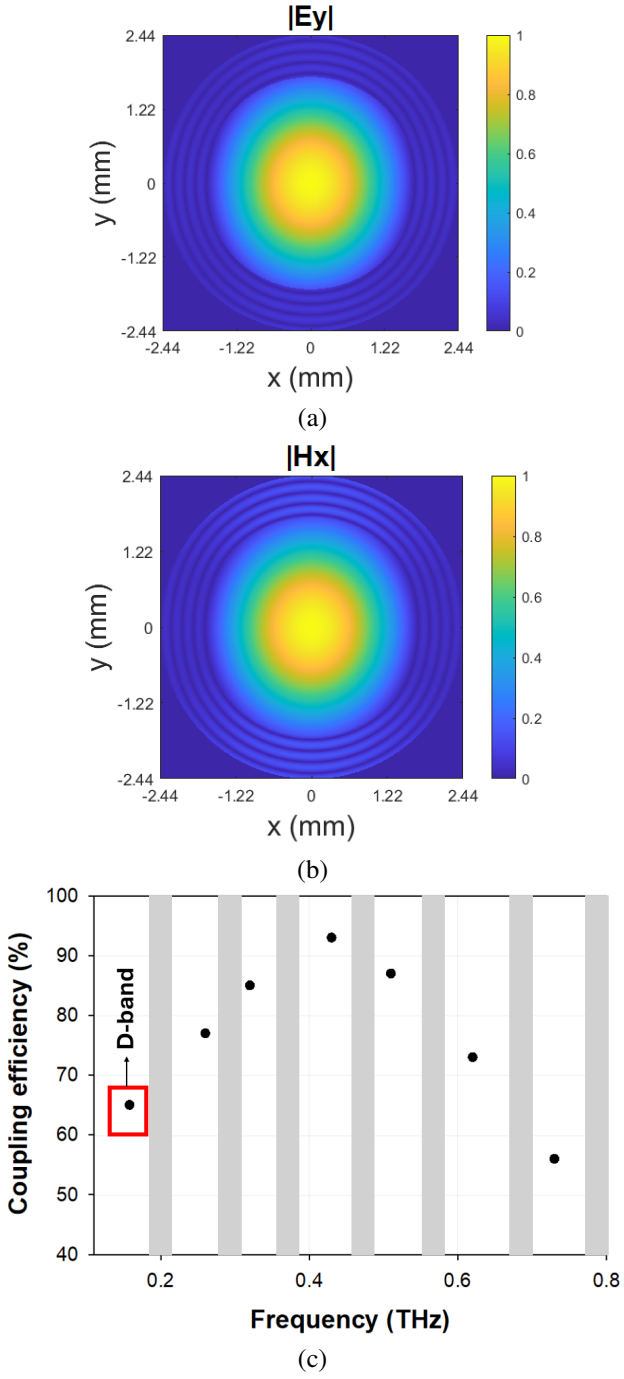


Figure 5: Fundamental mode characteristics of the proposed fiber: (a) normalized electric field distribution; (b) normalized magnetic field distribution; (c) coupling efficiency as a function of frequency.

3. Measured Results and Discussions

Following the numerical validation of the proposed design, fibers were fabricated and experimentally characterized to verify the predicted antiresonant guidance and transmission performance. This section summarizes the fiber fabrication process, measurement setup for fiber characterization, 3D-printing setup for Topas discs fabrication, fiber loss and coupling loss, and the influence of structural deformation and 3D printing resolution on transmission loss.

3.1. Fabrication process of the fiber and Topas characterization

The summary of the overall fabrication process, which includes the 3D-printing process step by step and wrapping up aluminium foil to act as a metallic layer is shown in Fig. 7(a). In this study, Prusa MK4S with 0.4 mm nozzle and CREAMELT® COC filaments are used for 3D printing. Three different lengths of fibers 3.82 cm, 6.67 cm and 9.80 cm are printed as shown in

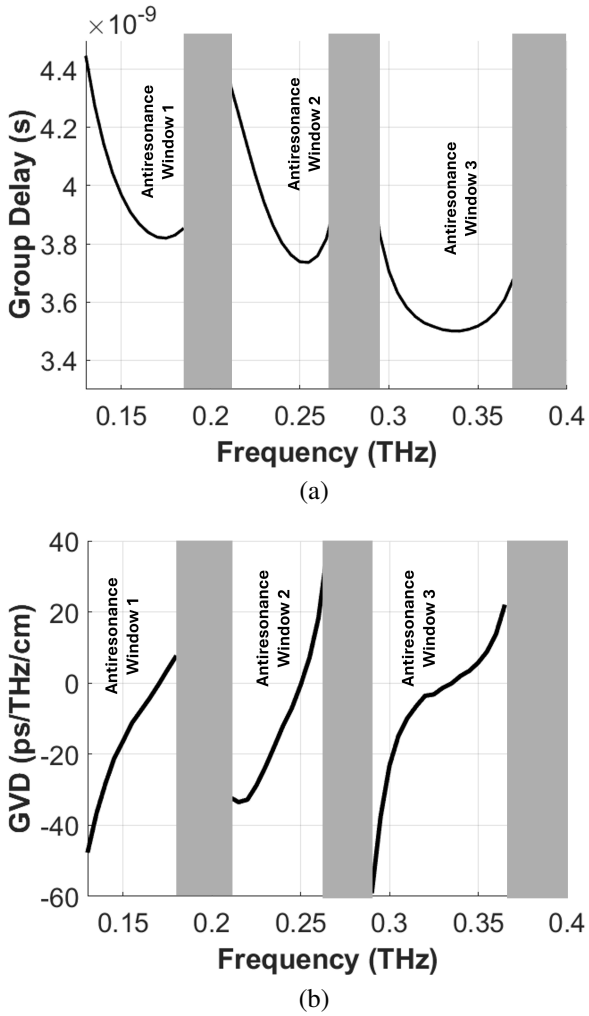


Figure 6: Simulated group delay and dispersion of the designed fiber: (a) group delay in the first three antiresonance windows; (b) dispersion in the first three antiresonance windows.

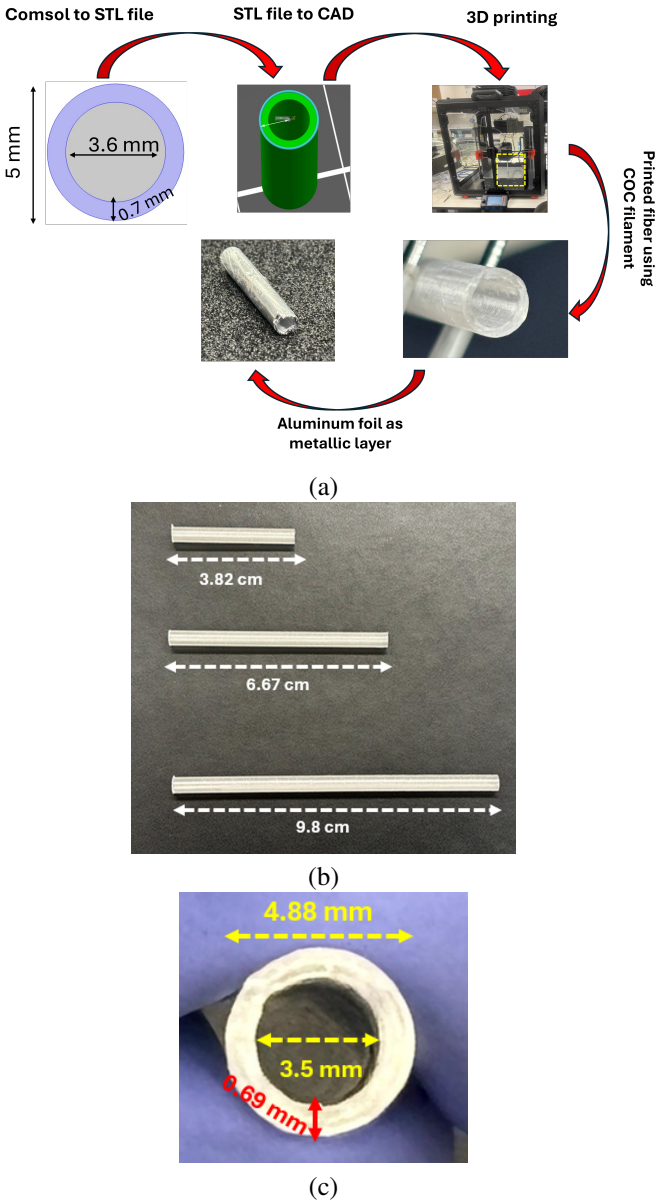


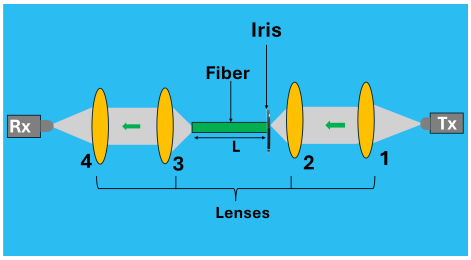
Figure 7: Fabrication and geometry of the 3D-printed fibers: (a) schematic illustration of the fabrication process; (b) fabricated fibers of different lengths; (c) cross-sectional view of a fabricated fiber.

Fig. 7(b). The printed fiber dimensions are slightly deformed compared to the calculated design. The outer diameter was reduced to 4.88 mm from 5 mm, and the core diameter was reduced to 3.5 mm from 3.6 mm, with a notch around the core, as shown in Fig. 7(c). The 3D printer setup was configured for more solid infill using a larger extrusion width, lower printing speed, and higher temperature. The material characterization aims to extract and represent the intrinsic properties of the Topas material itself rather than the properties of the porous printed structure. Here, intrinsic properties refer to the inherent properties of the bulk material (Topas), such as refractive index and absorption coefficient, while the porous printed structure contains an internal air gap, which may act as a medium for THz propagation.

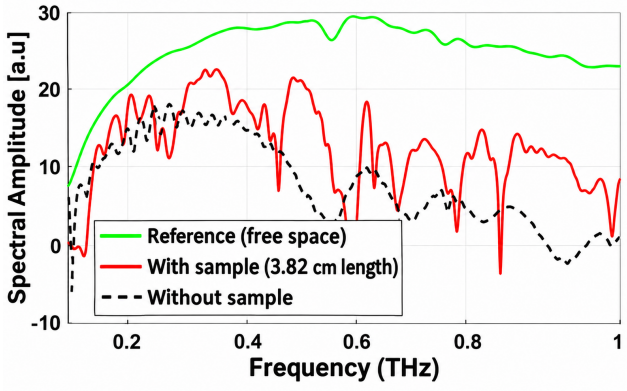
3.2. Experimental setup, metallic-coating validation and fiber characterization

Fiber characterisation was performed using a focused-beam THz-TDS setup, as shown in Fig. 8(a). To guide the terahertz beam through the fiber core, a circular aperture (iris) with a 3.5 mm opening was placed before the samples. The cut-off frequency of the iris is 42.9 GHz. The emitter generates a THz signal which transmits through the focused and collimated lenses as well as the sample. It can be seen from Fig. 8(b) that the fiber was characterized in three configurations: a free-space reference where there was no fiber between lenses 2 and 3, fiber-guided transmission where the fiber was placed between lenses 2 and 3 with a 50 mm focal range, and free-space propagation over an equivalent distance where there was no fiber. Measurements were repeated three times with 100 averages, showing good repeatability and confirming that the observed transmission was due to guidance by the designed fiber. Figure 8(b) also shows that the waterlines of the reference signal appeared at 0.55 THz, 0.75 THz, and 0.98 THz. The fiber was then tested

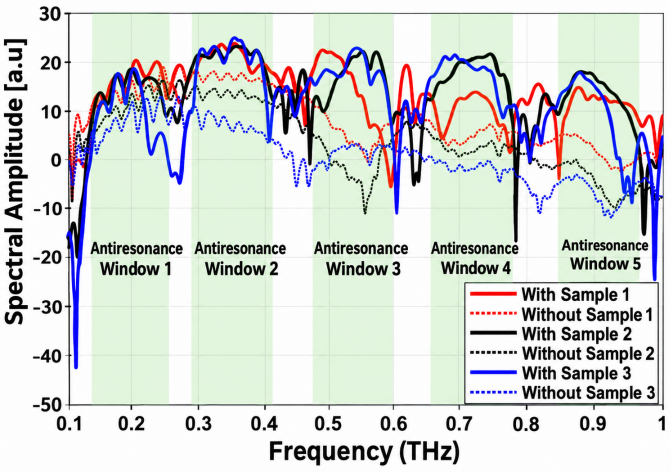
with and without a metallic layer to verify the effectiveness of the metallic coating. Here, samples 1, 2, and 3 are 3.82 cm, 6.67 cm, and 9.80 cm in length, respectively. The signal in the second, third, and fourth antiresonance regions has a higher amplitude compared to the signal in the first antiresonance region as shown in Fig. 8(c). It matches the theoretical concept because modal field confinement becomes stronger as the frequency increases, which makes the D_{core}/λ larger, whereas at lower frequencies the core size is smaller compared to the wavelength, which leads to leakage of light to nearby cladding. Due to the structural deformation of the printed samples, the resonance frequencies are shifted.



(a)



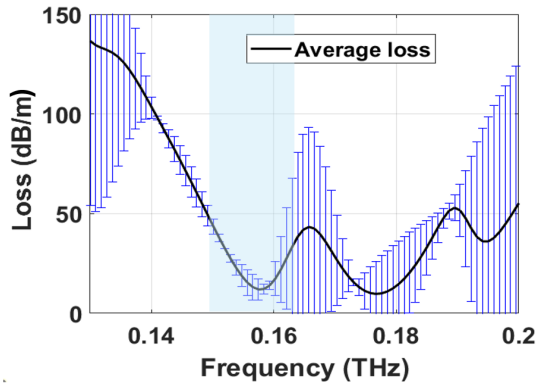
(b)



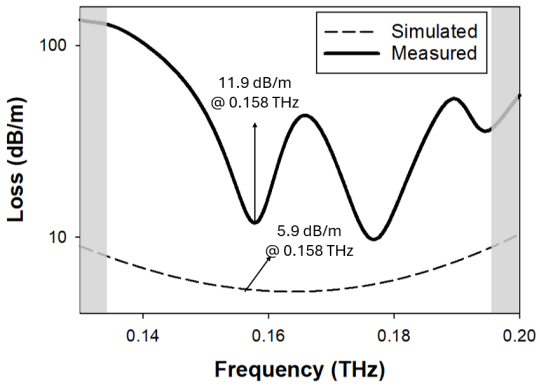
(c)

Figure 8: Experimental characterization of the fiber: (a) Schematic of the focused-beam TDS setup; (b) FFT transmission spectrum of sample 1 compared with the reference signal; (c) transmission spectra showing antiresonant regions for fibers of different lengths.

The fiber is designed in such a way that the targeted frequency range 0.13 - 0.17 THz is under antiresonance region. The average measured loss is 11.9 ± 5.3 dB/m at 0.158 THz as depicted in Fig. 9(a). The error margins are low at the antiresonance region and they get larger near the resonances. The lowest measured loss is 11.9 dB/m at 0.158 THz, while the simulated loss is 5.6 dB/m as shown in Fig. 9(b). Nevertheless, the measured loss is noticeably higher (almost twice) than the corresponding simulated loss. The experimental loss values were determined from the measured transmission response by assuming identical input and output coupling conditions for each fiber under optimum alignment. Several practical factors contribute to the increased measured loss. One important factor is the quality of the fiber end-face. Structural deformation affects the fiber transmission by generating additional unwanted resonances and shifting the transmissions. Next, producing a perfectly smooth and perpendicular cut in polymer fibers is difficult, which can lead to imperfect normal incidence of the terahertz beam into the fiber core. Furthermore, coupling efficiency plays a significant role in the overall loss performance. Similar discrepancies have also been reported in the literature, which are mainly associated with alignment tolerances and imperfections at the fiber end-face due to the structural deformations [13, 25, 26].



(a)



(b)

Figure 9: Loss comparison: (a) measured average loss with error bars of the proposed fiber design from 0.13 to 0.2 THz, where the frequency of interest is marked with a blue shaded box; (b) comparison of simulated and measured transmission loss.

The discrepancy between the simulated and measured loss can be partly attributed to fabrication-induced structural deformation. To investigate this effect, the printed fiber was numerically designed by introducing deformations in both the core and cladding surfaces as shown in Fig. 10. It has been observed that there are resonances introduced in the antiresonance regions due to the defective structure. A similar trend was observed in Fig. 9(a) for the measured loss, where there was a sharp peak at 0.17 THz, while the calculated resonance was at 0.19 THz. Consequently, there is resonance at 0.17 THz, which appeared due to the defective core and cladding (blue curve) as shown in Fig. 10.

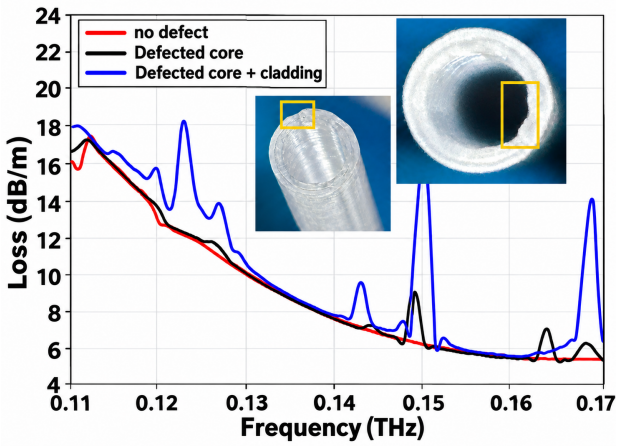


Figure 10: Simulated transmission loss for structures with core and cladding deformations based on the fabricated fiber geometry.

To study the impact of printing resolution on fiber loss and frequency of operation, the core radius was varied by 0.05 mm, corresponding to the resolution of the 3D printer used in our laboratory. For a fixed 5 mm outer-diameter fiber, a decrease in core size is equivalent to an increase in cladding thickness. From Fig. 11, it has been observed that as the cladding thickness (t) increases, the lower-frequency region of the spectrum exhibits higher loss. Moreover, a decrease in core size also leads to an increase in loss as the D_{core}/λ gets smaller, and there will be a higher power fraction in the polymer cladding, which increases the loss.

Table 1 compares the propagation loss accumulated over different fiber lengths with the corresponding coupling loss at 0.158 THz and 0.430 THz. For short fiber lengths, the total measured loss is dominated by coupling losses rather than propagation losses. At 0.158 THz, the coupling loss is 1.88 dB per end face (3.76 dB total), whereas the propagation loss is only 0.21 dB, 0.37 dB, and 0.55 dB for fiber lengths of 3.82 cm, 6.67 cm, and 9.80 cm, respectively. Based on the simulated propagation loss of 5.6 dB/m, a fiber length of approximately 67 cm is required for the accumulated propagation loss to exceed the total coupling loss at 0.158 THz. Similarly, at 0.430 THz, where the coupling loss is significantly lower (0.34 dB per end face, or 0.68 dB total), a minimum fiber length of approximately 19.1 cm is sufficient for the propagation loss to become the dominant loss mechanism. These results indicate

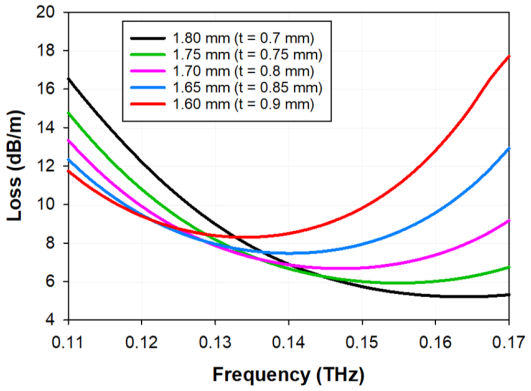


Figure 11: Transmission loss as a function of frequency for different core radii, illustrating the effect of 3D-printing resolution.

that, for the short fiber lengths used in this study, the measured transmission is strongly influenced by coupling losses, particularly in the D-band.

Table 1: Calculated propagation loss for different fiber lengths and corresponding coupling losses at 0.158 THz and 0.430 THz.

THz	Propagation Loss (dB)			Coupling
	$L = 3.82$ cm	$L = 6.67$ cm	$L = 9.80$ cm	Loss (dB)
0.158	0.21	0.37	0.55	3.76
0.430	0.14	0.24	0.35	0.68

As presented in Table 2, the proposed fiber demonstrates the smallest normalized core dimension ($D_{\text{core}}/\lambda = 1.89$) among previously reported 3D printed THz hollow-core fibers, indicating a highly compact structure with effective field confinement. Even with this reduced core size, the experimentally obtained loss of 11.9 dB/m at 0.158 THz remains comparable to other low-loss hollow-core fiber designs. For example, the structures reported in [25] and [13] achieve similar measured losses in the range of 12–16 dB/m but rely on considerably larger normalized core sizes of 13.8 and 4.93, respectively. Compared to these designs, the proposed fiber achieves a much smaller diameter while maintaining relatively lower loss characteristics. These results demonstrate that the proposed structure successfully balances compactness and low-loss guidance, highlighting its potential as an alternative to conventional copper interconnects.

4. Conclusion

In this study, we designed, fabricated, and experimentally characterized a circular-shaped HCF with an outer diameter of 5 mm for D-band operation, employing Topas as the dielectric material and aluminium foil as the metallic layer. The fabricated fiber achieved a measured loss of 11.9 dB/m at 0.158 THz, compared to a simulated loss of 5.6 dB/m. Additionally, within the 0.13–0.17 THz frequency range, the fiber exhibited a simulated group delay of 4.16 $\pm$ 0.81 ns and a dispersion of -36.5 ± 20 ps/THz/cm. This paper also analyzes coupling efficiency, offering further insight into input coupling and the over-

Table 2: Comparison of performance metrics for reported 3D-printed THz hollow-core fibers.

Ref	Freq. (THz)	D_{core}/λ	Measured loss (dB/m)	Simulated loss (dB/m)
[10]	0.53	8.83	40 @ 0.53 THz	Not reported
[26]	0.39–0.5	8.47	21.71–52.1	17.736–65.1
[13]	0.28	4.93	16 @ 0.28 THz	15 @ 0.280 THz
[25]	0.46	13.8	12.16	8.7
This work	0.13–0.17	1.89	11.9 @ 0.158 THz	5.6 @ 0.158 THz

all loss mechanism. Five distinct antiresonance transmission windows were also experimentally observed. The discrepancies between the experimental and simulated results are primarily attributed to the fiber deformation during the fabrication process. To the best of the authors' knowledge, the proposed fiber demonstrates the miniaturized structural dimensions and normalized core size ($D_{\text{core}}/\lambda = 1.89$) among recently reported 3D-printed hollow-core fibers operating in the sub-THz regime, while maintaining competitive transmission loss performance. This work numerically showed the effectiveness of a metallic coating in compensating leakage caused by compact dimensions. The proposed fiber diameter (5 mm) represents an important step toward the development of compact HCF technologies for THz communications. Its dimensions fall within the lower range of commercially available coaxial cables, which typically have outer diameters ranging from 2.54 mm to 31.75 mm. The obtained results demonstrate that metallic-assisted confinement provides an effective route towards compact, low-loss THz hollow-core fibers, enabling substantial miniaturization without the severe transmission penalties typically associated with small-core designs. Future work will focus on fabricating the circular HCF using an extrusion-based approach and benchmarking its performance against the proposed 3D-printed design, especially for longer lengths of fiber with smoother surfaces and reduced structural deformation.

Acknowledgment

This research was supported by the Australian Government through the Australian Research Council (ARC) Linkage Projects funding scheme (LP210200524). The authors acknowledge Dr. Parisa Yadranjee Aghdam (Ericsson, Gothenburg) for her constructive feedback and valuable suggestions, which contributed to the refinement of this work. Heike Ebendorff-Heidepriem acknowledges support through a South Australian Future Industry Making Fellowship. Lastly, the authors would like to acknowledge Dr. Qigejian Alfred Wang and Dr. Dominik Walter Vogt from Terahertz Innovation Group for their assistance and feedback in the coupling efficiency calculation and analysis.

References

[1] S. Parkvall, R. Baldemair, E. Eriksson *et al.*, "A concept for evaluating sub-Thz communication for future 6G," *Ericsson and Intel Corporation*, 2023.

[2] S. Atakaramians, "Terahertz waveguides: the fundamental component for future world connectivity," *2024 49th International Conference on Infrared, Millimeter, and Terahertz Waves (IRMMW-THz)*, pp. 1–1, 2024. [Online]. Available: https://api.semanticscholar.org/CorpusID:273219682

[3] J. Ma, Y. Song, M. Zhang, G. Liu, W. Li, J. F. Federici, and D. M. Mittleman, "Terahertz channels in atmospheric conditions: Propagation characteristics and security performance," *Fundamental Research*, vol. 5, no. 2, pp. 526–555, 2025.

[4] Q. Wang, Y. Deng, D. Mishra, Y. Xie, E. Aboutanios, and S. Atakaramians, "Demonstration of photonics-based D-band integrated localization and communication," *Appl. Opt.*, vol. 63, no. 15, pp. 4068–4076, May 2024. [Online]. Available: https://opg.optica.org/ao/abstract.cfm?URI=ao-63-15-4068

[5] S. Atakaramians, S. A. V., H. Ebendorff-Heidepriem, M. Nagel, B. M. Fischer, D. Abbott, and T. M. Monro, "Thz porous fibers: design, fabrication and experimental characterization," *Opt. Express*, vol. 17, no. 16, pp. 14 053–14 062, Aug 2009. [Online]. Available: https://opg.optica.org/oe/abstract.cfm?URI=oe-17-16-14053

[6] S. Atakaramians, S. A. V., T. M. Monro, and D. Abbott, "Terahertz dielectric waveguides," *Adv. Opt. Photon.*, vol. 5, no. 2, pp. 169–215, Jun 2013. [Online]. Available: https://opg.optica.org/aop/abstract.cfm?URI=aop-5-2-169

[7] H. Li, Y. Cao, M. Skorobogatiy, and S. Atakaramians, "Terahertz fiber devices," *APL Photonics*, vol. 10, no. 2, p. 021101, 02 2025. [Online]. Available: https://doi.org/10.1063/5.0239310

[8] H. Zou, J. Zhou, Y. Lu, Y. Du, R. Zhang, and D. Zhou, "Ultra-low loss, single polarization hollow-core antiresonant fiber," *Journal of the Optical Society of America B*, vol. 41, no. 5, pp. 1134–1143, 2024.

[9] S. K. Noor, M. Gu, S. An, P. Aghdam, H. Ebendorff-Heidepriem, and S. Atakaramians, "Antiresonant fibers for 6G communication," in *2024 49th International Conference on Infrared, Millimeter, and Terahertz Waves (IRMMW-THz)*. IEEE, 2024, pp. 1–2.

[10] J. Sultana, M. S. Islam, C. M. Cordeiro, M. S. Habib, A. Dinovitser, M. Kaushik, B. W.-H. Ng, H. Ebendorff-Heidepriem, and D. Abbott, "Hollow core inhibited coupled antiresonant terahertz fiber: A numerical and experimental study," *IEEE transactions on terahertz science and technology*, vol. 11, no. 3, pp. 245–260, 2020.

[11] L. Van Putten, J. Gorecki, E. Numkam Fokoua, V. Apostolopoulos, and F. Poletti, "3D-printed polymer antiresonant waveguides for short-reach terahertz applications," *Applied optics*, vol. 57, no. 14, pp. 3953–3958, 2018.

[12] S. Yang, X. Sheng, G. Zhao, Y. Wang, and Y. Yu, "Novel pentagram Thz hollow core anti-resonant fiber using a 3D

printer," *Journal of Infrared, Millimeter, and Terahertz Waves*, vol. 40, no. 7, pp. 720–730, 2019.

[13] Q. Mu, Y. Zhu, D. Kong, Z. He, H. Liu, and L. Wang, "Design, simulation, and characterization of a partial negative curvature antiresonant hollow-core fiber for low loss terahertz wave transmission," *IEEE Transactions on Terahertz Science and Technology*, vol. 14, no. 4, pp. 510–518, 2024.

[14] B. Bowden, J. A. Harrington, and O. Mitrofanov, "Low-loss modes in hollow metallic terahertz waveguides with dielectric coatings," *Applied physics letters*, vol. 93, no. 18, 2008.

[15] M. S. Islam, C. M. Cordeiro, M. J. Nine, J. Sultana, A. L. Cruz, A. Dinovitser, B. W.-H. Ng, H. Ebendorff-Heidepriem, D. Losic, and D. Abbott, "Experimental study on glass and polymers: Determining the optimal material for potential use in terahertz technology," *IEEE access*, vol. 8, pp. 97 204–97 214, 2020.

[16] S. K. Noor, M. Gu, S. An, H. Ebendorff-Heidepriem, D. Mishra, and S. Atakaramians, "Hollow-core waveguide for d-band: A low-profile 3d-printed design," in *2026 20th European Conference on Antennas and Propagation (EuCAP)*, 2026, pp. 1–5.

[17] M. Kaluza, M. Walczakowski, P. Komorowski, and A. Siemion, "Influence of 3d printing parameters on the thz optical properties of coc material," in *2024 49th International Conference on Infrared, Millimeter, and Terahertz Waves (IRMMW-THz)*, 2024, pp. 1–2.

[18] D. Pozar, *Microwave Engineering*. Wiley, 2011. [Online]. Available: https://books.google.bs/books?id=_YEbGAXCcAMC

[19] J. M. Bennett, "Precise method for measuring the absolute phase change on reflection," *Journal of the Optical Society of America*, vol. 54, no. 5, pp. 612–624, 1964.

[20] E. Hecht, *Optics*, 5th ed. Pearson Education, 2017.

[21] G. Hou, S. Liu, Y. Zhu, S. Yu, Z. Zha, Q. Zhao, S. Liu, C. Jing, and J. Chu, "Fabrication of Ag/PP terahertz hollow waveguide by vacuum evaporation method and transmission performance investigations," *Optical Materials*, vol. 147, p. 114710, 2024. [Online]. Available: https://www.sciencedirect.com/science/article/pii/S092534672301282X

[22] R. Cables. (2025) Rf cables–coaxial cable selection guide. [Online]. Available: https://www.rfcables.org/articles/19.html

[23] A. W. Snyder, "Coupled-mode theory for optical fibers," *J. Opt. Soc. Am.*, vol. 62, no. 11, pp. 1267–1277, Nov 1972. [Online]. Available: https://opg.optica.org/abstract.cfm?URI=josa-62-11-1267

[24] Q. Wang, S. D. A. Shah, H. Li, B. Kuhlmey, and S. Atakaramians, "20 dB improvement utilizing custom-designed 3D-printed terahertz horn coupler," *Opt. Express*, vol. 31, no. 1, pp. 65–74, Jan 2023. [Online]. Available: https://opg.optica.org/oe/abstract.cfm?URI=oe-31-1-65

[25] L. Li, D. Lin, F. Meng, Y. Zhao, Y. Cui, Y. Cao, H. Liu, H. Mu, Y. Niu, J. He *et al.*, "Investigation on low-loss hollow-core anti-resonant terahertz fiber," *Applied Optics*, vol. 62, no. 21, pp. 5778–5785, 2023.

[26] L. Xue, X. Sheng, S. Lou, G. Zhao, S. Yang, Z. Xing, and H. Jia, "High-birefringence low-loss hollow-core thz waveguide embedded parallel slab cladding," *IEEE Transactions on Terahertz Science and Technology*, vol. 12, no. 5, pp. 471–480, 2022.